



ELSEVIER

Available online at www.sciencedirect.com

ScienceDirect

journal homepage: www.elsevier.com/locate/he

Enhanced gaseous hydrogen solubility in ferritic and martensitic steels at low temperatures

Andreas Drexler ^{a,*}, Florian Konert ^b, Oded Sobol ^b, Michael Rhode ^b,
Josef Domitner ^a, Christof Sommitsch ^a, Thomas Böllinghaus ^b

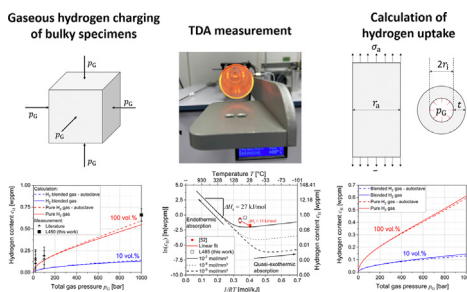
^a Graz University of Technology, Institute of Materials Science, Joining and Forming, Research Group of Lightweight and Forming Technologies, Inffeldgasse 11/I, 8010 Graz, Austria

^b Bundesanstalt für Materialforschung und -prüfung (BAM), Department 9 – Component Safety, Unter Den Eichen 87, 12205 Berlin, Germany

HIGHLIGHTS

- Improvement of Sievert's law to consider trapping sites and stress states.
- Calculation and validation of gaseous hydrogen solubility under extreme conditions.
- Hydrogen uptake measured for L450 steel at 200 and 1000 bar.
- Calculation of the hydrogen solubility in pipes and pressure vessels.
- Comprehensive literature survey of gaseous hydrogen solubility.

GRAPHICAL ABSTRACT



ARTICLE INFO

Article history:

Received 9 June 2022

Received in revised form

31 August 2022

Accepted 11 September 2022

Available online xxx

Keywords:

Steel

Hydrogen gas

ABSTRACT

Metals that are exposed to high pressure hydrogen gas may undergo detrimental failure by embrittlement. Understanding the mechanisms and driving forces of hydrogen absorption on the surface of metals is crucial for avoiding hydrogen embrittlement. In this study, the effect of stress-enhanced gaseous hydrogen uptake in bulk metals is investigated in detail. For that purpose, a generalized form of Sievert's law is derived from thermodynamic potentials considering the effect of microstructural trapping sites and multiaxial stresses. This new equation is parametrized and verified using experimental data for carbon steels, which were charged under gaseous hydrogen atmosphere at pressures up to 1000 bar. The role of microstructural trapping sites on the parameter identification is critically discussed.

* Corresponding author.

E-mail address: andreas.drexler@tugraz.at (A. Drexler).

<https://doi.org/10.1016/j.ijhydene.2022.09.109>

0360-3199/© 2022 The Author(s). Published by Elsevier Ltd on behalf of Hydrogen Energy Publications LLC. This is an open access article under the CC BY license (<http://creativecommons.org/licenses/by/4.0/>).

Pressure-dependent solubility
Sievert's law
Hydrogen trapping
Thermodynamic modelling

Finally, the parametrized equation is applied to calculate the stress-enhanced hydrogen solubility of thin-walled pipelines and thick-walled pressure vessels during service.

© 2022 The Author(s). Published by Elsevier Ltd on behalf of Hydrogen Energy Publications LLC. This is an open access article under the CC BY license (<http://creativecommons.org/licenses/by/4.0/>).

Introduction

Green gaseous hydrogen is one of the most promising energy carriers in near future [1]. Thermal combustion of pure hydrogen gas is clean, as it produces only water. Hydrogen gas is also used in fuel cell systems converting the stored chemical energy into electricity. However, at atmospheric pressure of 1 bar and temperature of 25 °C, hydrogen gas has relatively low volumetric energy density (12.7 MJ/m³), especially compared to methane (40 MJ/m³), which is the main constituent of natural gas [2]. In order to distribute large volumes of gaseous hydrogen in a cost-efficient way [3], compression or liquification of the gas is required [2], which increase the volumetric energy density to a practical level [4]. Hydrogen partial pressures up to 200 bar are common in industry (e.g. for storage in gas bottles), while pressures up to 1000 bar will be considered in future to increase the energy density (e.g. for compressed hydrogen tube trailers [5] or gas stations). One of the challenges for using gaseous hydrogen is establishing reliable and safe structures including pipelines and pressure vessels for transmission and storage. However, in particular high-strength steels exposed to hydrogen gas at high pressures may suffer from loss in ductility and strength, which is known as hydrogen embrittlement (HE) [6]. Different mechanisms of macroscopic brittle and time-delayed HE have been explained based on microplasticity or atomistic theories [7–9]. However, even after more than 100 years of research in this field [10] no conclusive theory is available in literature. Some authors [11] proposed a simultaneous contribution of different “classical” mechanisms, such as hydrogen-enhanced localized plasticity (HELP) and hydrogen-enhanced decohesion (HEDE). For example, HEDE possibly predominates for intergranular fracture, while HELP contributes to dimpled fracture. Other authors including Lynch [12], Nagumo [13] or Kirchheim [14] proposed new aspects of hydrogen-related failures to improve the understanding of the rate dependency [15,16] and of different occurrence of fracture surfaces, such as cleavage-like morphologies, depending on hydrogen content and stress intensity [17]. Anyway, each of the proposed HE mechanisms suppose atomic hydrogen absorption on the surface to reach the critical hydrogen content of the material [18,19]. In case of hydrogen gas, high driving forces are necessary to dissociate hydrogen molecules [20,21] and to diffuse hydrogen atoms into the bulk. Under equilibrium conditions, the analytical calculation of the hydrogen solubility c_H within a given material requires the environmental hydrogen partial pressure p_{H_2} and the temperature T of the investigated system. Sievert's law [22,23] allows calculating the equilibrium hydrogen content at high temperatures or low partial pressures [24,25]:

$$c_H = K \sqrt{p_{H_2}} \quad (1)$$

K is the temperature-dependent equilibrium coefficient. Nevertheless, at high pressures and low temperatures “real” hydrogen gas behavior becomes crucial and the hydrogen partial pressure must be replaced by the fugacity f [25]. The entry of hydrogen into steels causes a small expansion of the lattice volume. Thus, the hydrogen absorption is affected by elastic stress fields which can be related to the increase of the hydrogen solubility [18,26,27]:

$$\frac{c_H}{c_{H,0}} = \exp\left(\frac{\sigma_1 V_H}{3RT}\right) \quad (2)$$

c_H and $c_{H,0}$ are the hydrogen solubilities in the stressed and unstressed material at identical partial pressure, σ_1 is the uniaxial tensile stress, V_H is the partial molar volume of interstitial lattice sites and R is the universal gas constant. However, the roles of multiaxial stresses and microstructure on the hydrogen solubility of steels at low temperatures and high gas pressures need further investigations. Microstructures of high-strength steels contain high densities of trapping sites which increase the hydrogen solubility.

For that reason, the present work aims to derive a new thermodynamic relationship for gaseous hydrogen solubility from generalized chemical potentials. This new relationship considers the influence of trap densities, binding energies, temperature, fugacity and hydrostatic stresses. Parametrization was performed using experimental data. Applying a simple single-trap approach enabled the reasonable calculation of hydrogen solubility for a wide range of carbon steels at low temperatures and gas pressures up to 1000 bar. The new findings improve the basic understanding of material tests performed at low temperatures and high gas pressures on lab scale. Based on these tests the influence of hydrogen-containing gas mixtures on structural steel components and the hydrogen solubility in steel for pipeline and pressure vessels during service were studied.

Analytical model

Gaseous hydrogen absorption

Absorption of diatomic hydrogen gas molecules H_2 at the metal surface can be described by the reversible reaction



where V_L represents a vacant interstitial lattice site next to the surface and H_L is a freely diffusive lattice hydrogen atom in the metal phase. V_L can also be neglected in Eq. (3), if the number of interstitial lattice sites is much higher than the number of absorbed lattice hydrogen atoms. Only the interstitial lattice sites are assumed to contribute to the dynamic

exchange with the environmental gas phase. A vacant interstitial lattice site is necessary, that an adsorbed hydrogen atom can jump from the surface into bulk. Once hydrogen is absorbed by the interstitial lattice, it diffuses into the metal and can be trapped at a microstructural defect site [28], which can be expressed as



where V_T is a vacant trapping site and H_T is a trapped hydrogen atom. For simplification, it is assumed that V_T is directly accessible from the crystal lattice [29], which is fulfilled for, e.g., vacancies, dislocations and carbide interfaces. Especially trapping plays a crucial role in steels [30], as it increases the local hydrogen solubility and decreases the chemical diffusion coefficient [31,32]. This will be discussed in more detail in section 2.2. As illustrated schematically in Fig. 1, a hydrogen atom must pass different energy states for being absorbed in the metal phase. In thermodynamic equilibrium, the hydrogen content absorbed in the metal phase is constant for a given temperature and hydrogen partial pressure. This hydrogen content only depends on the solution enthalpy ΔH_s , which represents the heat release per bulk of absorbed hydrogen atom. In the present paper, the solution enthalpy is negative for an exothermic reaction ($\Delta H_s < 0$) and positive for an endothermic absorption ($\Delta H_s > 0$). According to the theory of chemical kinetics, the energy states at the surface only affect the absorption rates, but do not change the hydrogen content in thermodynamic equilibrium. This equilibrium content is named hydrogen solubility throughout the entire work. Different to the work of San Marchi et al. [25], hydrogen solubility includes both lattice and trapped hydrogen atoms and, thus, represents the hydrogen content as determined by extractive hydrogen measuring methods. For gas mixtures (e.g., hydrogen blended methane), the solubility of hydrogen can be assumed as unaffected, as long as the gas mixture does not dissociate and interact with the hydrogen molecules. If this is case, the gas mixture behaves like an ideal gas.

Hydrogen in metals

Assuming that hydrogen can diffuse freely in the crystal lattice where it is trapped at microstructural defects [33] (e.g. grain boundaries, dislocations and vacancies). Thus, the total molar hydrogen concentration c includes the lattice concentration c_L and the trap concentration c_T :

$$c = c_L + c_T \quad (5)$$

The total hydrogen content c_H in wppm can be calculated from the total molar concentration in mol/mm³ using $c_H = 10^6 \cdot M c / \rho$. M is the molar mass of hydrogen (1.008 g/mol) and ρ is the density of steel ($7.9 \cdot 10^{-3}$ g/mm³). The density of lattice sites, N_L , and the density of trap sites, N_T , are constant in the present work, which allows defining the lattice site fraction $y_L = c_L / N_L$ and the trap site fraction $y_T = c_T / N_T$. Both site fractions, y_L and y_T , can take values from zero to unity depending on the solution enthalpy ΔH_s [25] and on the binding energy E_b [34]. In ferritic iron crystals, interstitial lattice hydrogen can either occupy tetrahedral or octahedral sites. According to Kholobina et al. [29], the calculated solution enthalpy ΔH_s of tetrahedral sites (0.22 eV or 21.2 kJ/mol) is smaller than of octahedral sites (0.37 eV or 35.7 kJ/mol). Hence, the occupation of tetrahedral sites in ferritic iron is preferred at low temperatures [9]. Nevertheless, octahedral sites are thermally activated if the temperature increases. E_b of different crystal defects has been well studied in the last decades [28,31,35,36], and typical values are in the range from 0 to about 100 kJ/mol in ferritic or martensitic steels. E_b depends on the type of defect, on the change of interatomic forces between hydrogen and iron at the defect sites with respect to interstitial lattice sites, and on the dilation of the crystal lattice in the immediate vicinity of crystal defects. Hydrogen in steels can be treated as ideal solution interacting with the hydrostatic stress field on the macroscale [18,37] as well as on the microscale [18,38]. Micro-residual stresses [39] are in the range of the Young's modulus E and, thus, these stresses are one magnitude larger than macrostresses. While

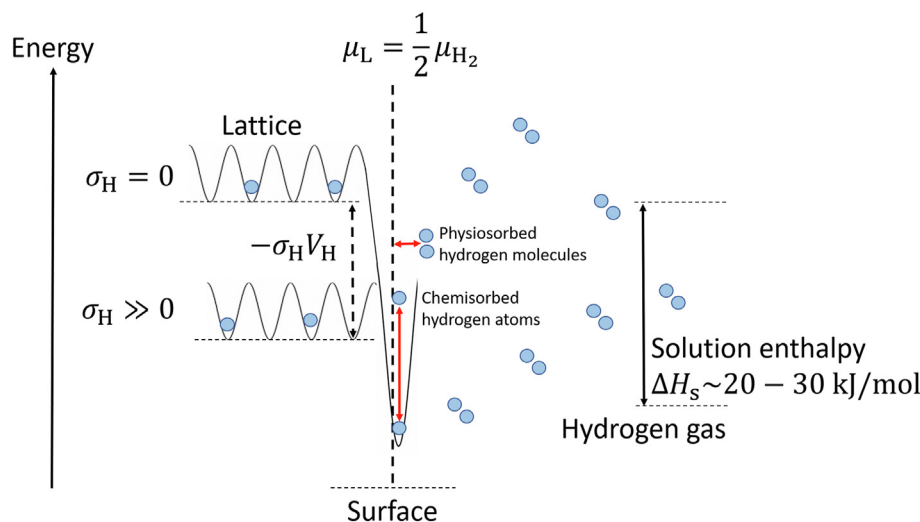


Fig. 1 – Sketch of the hydrogen energy states in a metal-gas equilibrium.

hydrostatic tension dilates the crystal lattice and increases the lattice hydrogen concentration, hydrostatic compression of the lattice decreases the lattice hydrogen concentration [40]. For instance, Hussein et al. [41] demonstrated how heterogeneous fields of microstresses contribute to hydrogen segregation at grain boundaries. In thermodynamic equilibrium, Oriani's theory applies [33,42] and the trapped hydrogen concentration can be calculated from the lattice concentration at given temperature T as

$$c_T = y_T N_T = \frac{y_L N_T}{K_T + y_L (1 - K_T)} \quad (6)$$

$K_T = \exp(-E_b/RT)$ is the inverse equilibrium constant resulting from Eq. (4) by applying the law of mass action [28]. Inserting Eq. (6) into Eq. (5) yields the total molar hydrogen concentration c as function of the lattice concentration c_L [42]:

$$c = \left(1 + \frac{N_T}{N_L} \frac{1}{K_T + y_L (1 - K_T)}\right) c_L \quad (7)$$

According to Kirchheim [43], Eq. (7) can be simplified in practice as

$$c \approx \frac{N}{N_L} \left(1 + \frac{N_T}{N} \frac{1}{K_T}\right) c_L = g(N_L, N_T, K_T) c_L \quad (8)$$

$N = N_L + N_T$ is to the total number of possible hydrogen positions in the microstructure per volume unit. Fig. 2 compares calculations of c by using Eq. (7) and Eq. (8). Similar results were obtained from both equations, if $N_T \ll N_L$, $y_L \ll K_T$ and $K_T \ll 1$ [42], which is fulfilled for binding energies less than 40 kJ/mol and for $y_L = 1.2 \cdot 10^{-7}$.

Hydrogen solubility

This section presents a newly established relationship between hydrogen solubility c_H , microstructure, multiaxial stress state, temperature and gas pressure, which is derived based on thermodynamic expressions. In thermodynamic

equilibrium, the generalized chemical potentials of environmental diatomic hydrogen molecules, μ_{H_2} , and of hydrogen atoms dissolved in ferritic iron, μ_L , must be equal:

$$\frac{1}{2} \mu_{H_2} = \mu_L \quad (9)$$

Considering the activity of real hydrogen gas as $f = p_{H_2} \gamma$, which is apparent at high pressures and low temperatures, the generalized chemical potential of environmental hydrogen molecules is

$$\mu_{H_2} = \mu_{H_2,0} + RT \ln f \quad (10)$$

γ is the fugacity coefficient. Based on the Abel-Noble relationship, San Marchi et al. [25] derived a simple analytical expression for the fugacity coefficient,

$$\gamma = \exp\left(\frac{p_{H_2} b}{RT}\right) \quad (11)$$

where b represents the constant finite volume of hydrogen gas molecules (van der Waals constant). Basically, all gases behave ideal at very low pressures ($p \ll 1$ bar) and the fugacity coefficient γ , as defined in Eq. (11), needs to converge to unity. Since atomic hydrogen dissolved in ferritic iron can be treated as ideal solution, the generalized chemical potential μ_L [38,42,44,45] is

$$\mu_L = \mu_{L,0} + RT \ln y_L - \sigma_H V_H \quad (12)$$

σ_H is the hydrostatic stress which is 1/3 of the trace of the stress tensor σ_{ij} . The first terms $\mu_{H_2,0}$ and $\mu_{L,0}$ in Eq. (10) and Eq. (12), respectively, are the temperature-dependent chemical potentials of pure hydrogen molecules and atoms, respectively, and the second term corresponds to the entropy of mixture. The third term results from the energy gain by hydrogen diffusing to distorted interstitial lattice sites [46]. Inserting Eqs. (10) and (12) into Eq. (9) yields

$$\frac{1}{2} \mu_{H_2,0} + RT \ln = \mu_{L,0} + RT \ln y_L - \sigma_H V_H \quad (13)$$

which can be reformulated to

$$RT \ln \sqrt{f} - RT \ln y_L + \sigma_H V_H = \mu_{L,0} - \frac{1}{2} \mu_{H_2,0} \quad (14)$$

The right-hand side of Eq. (14) describes the change of the solution enthalpy ΔH_s and of the entropy ΔS as $\mu_{L,0} - \frac{1}{2} \mu_{H_2,0} = \Delta H_s - T \Delta S$. Hence, one can directly write

$$RT \ln \left(\frac{\sqrt{f}}{y_L}\right) = \Delta H_s - \sigma_H V_H - T \Delta S \quad (15)$$

Solving Eq. (15) for the lattice hydrogen concentration c_L yields the following analytical expression

$$c_L = y_L N_L = K'_0 \sqrt{f} \exp\left(-\frac{\Delta H_s - \sigma_H V_H}{RT}\right) \quad (16)$$

where the pre-factor K'_0 is constant. Combining Eq. (16) with Eq. (8) allows expressing the solubility c_H of a metal in thermodynamic equilibrium as

$$c_H = K_0 \sqrt{f} \exp\left(-\frac{\Delta H_s - \sigma_H V_H}{RT}\right) \quad (17)$$

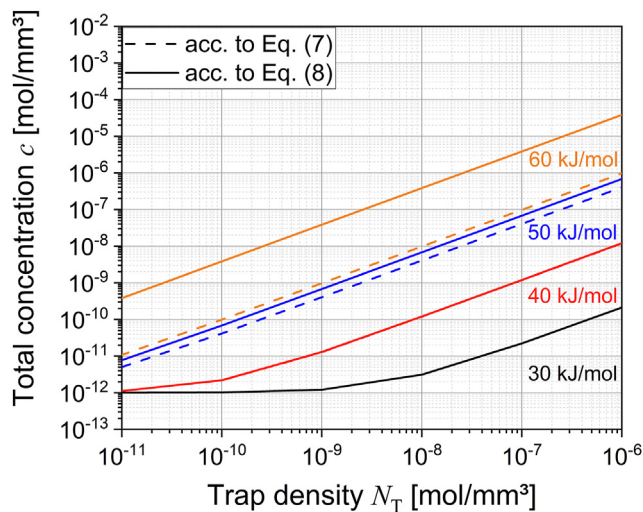


Fig. 2 – Comparing calculations of the total hydrogen concentration according to Eqs. (7) and (8).

Throughout this work $K_0 \cong K'_0 \cdot g(N_L, N_T, K_T)$ is the solubility coefficient and the term $\Delta H_s - \sigma_H V_H$ is the effective solution enthalpy. Eq. (17) is an analytical expression of the hydrogen solubility relating the hydrogen content of a metal to the partial pressure of hydrogen, to the temperature, to the microstructural trapping capacity of the metal and to the multiaxial stress state. Introducing the equilibrium coefficient $K = K_0 \exp\left(-\frac{\Delta H_s - \sigma_H V_H}{RT}\right)$, one can write Eq. (17) directly in a more simplified form as

$$c_H = \sqrt{f}K \quad (18)$$

Obviously, if the hydrostatic stress is zero, at high temperatures and at low partial pressures, Eq. (18) becomes Sievert's law [22,23].

Mechanical problem

Multiaxial stresses σ_i are induced below the surface of structural components (e.g., pipes) exposed to environmental gas pressure p_G . The total gas pressure is the sum of the partial pressures of different gas species. Neglecting interaction between the different molecules, the partial pressure is the pressure a single gas species would have, if it would occupy the entire volume at given temperature without the presence of any other species. In the present work, the hydrogen partial pressure p_{H_2} is either 10% or 100% of p_G . While a hydrogen partial pressure of 10% of p_G may already exist in state-of-the-art natural gas grids, grids for distributing pure hydrogen gas of 100% of p_G will be built in near future. For relating the gas pressure to the mechanical stress state in a certain specimen or component, respectively, analytical equations were collected in Table 1 [47]. All equations assume linear elastic material behavior and thus, the effect of plastic yielding on the gaseous hydrogen solubility [15,48] was not considered in the calculations. The role of stress-enhanced hydrogen solubility is studied for three different cases:

1. Externally pressurized bulky specimens,
2. Internally pressurized thin-walled pipes (up to 200 bar) and
3. Internally pressurized thick-walled pressure vessels (up to 1000 bar).

Gas charging of bulky specimens on laboratory scale causes compressive stresses which are equal to the outer gas pressure, $\sigma_i = -p_G$, where σ_i is the principal stress in each of the three directions i . The compressive stresses are homogeneously distributed within the specimens and they are independent from the shape and size of the specimens. The compressive hydrostatic stress σ_H decreases linearly with increasing gas pressure p_G , as illustrated in Fig. 3. According to the basics of plasticity theory, a homogenous outer pressure cannot cause any plastic yielding and thus the equivalent stress according to von Mises σ_{eq} in the specimens is zero, as shown in Fig. 3. Anyway, the effect of the hydrostatic compressive stress is neglected in the experimental evaluation of gaseous hydrogen uptake of bulky specimens using autoclave systems. Therefore, for comparing theoretical and experimental results it is necessary to define the stress-free state of $\sigma_H = 0$ as reference throughout this work.

Due to the cylindrical symmetry of pipes, stress components σ_i act in different directions, namely in radial, r , tangential, t , and axial, a , directions. In case of linear elastic material behavior, analytical expressions exist for each of the stress components σ_r , σ_t and σ_a [47]:

$$\sigma_r = -\frac{\left(\frac{r_a}{r}\right)^2 - 1}{\left(\frac{r_a}{r_1}\right)^2 - 1} p_G, \quad \sigma_t = \frac{\left(\frac{r_a}{r}\right)^2 + 1}{\left(\frac{r_a}{r_1}\right)^2 - 1} p_G \quad \text{and} \quad \sigma_a = \frac{r_1}{2t} p_G \quad (19)$$

r is the radius, r_1 is the inner radius and r_a is the outer radius of the pipe. Whenever $\frac{t}{2r_0} \ll 1$, Barlow's equations [47] can be applied and Eq. (19) are simplified to

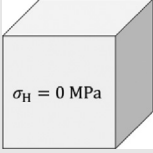
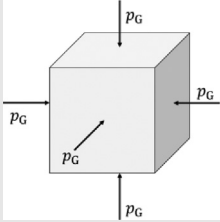
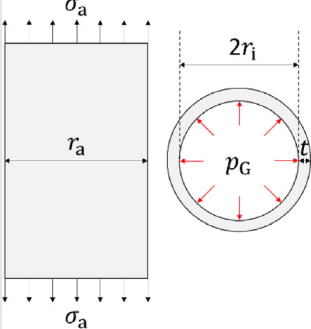
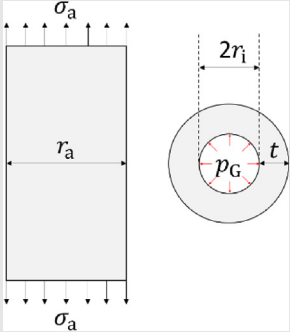
$$\sigma_r = 0, \quad \sigma_t = \frac{r_0}{t} p_G \quad \text{and} \quad \sigma_a = \frac{r_1}{2t} p_G \quad (20)$$

where $t = r_a - r_1$ is the thickness of the pipe wall and $r_0 = (r_a - r_1)/2$ is the average pipe radius. Barlow's equations are considered in various standards such as DIN EN 13480 and DIN EN 13445 to determine dimensions of pipelines or pressure vessels.

In Fig. 4a the stress components σ_i acting in different directions are plotted as function of the radius r at the internal gas pressure of $p_G = 100$ bar. Realistic pipeline dimensions with the inner radius of $r_1 = 400$ mm and the outer radius of $r_a = 410$ mm are applied. Hence, the wall thickness $t = 10$ mm and the ratio $t/2r_0 = 0.012$ are considered. According to Barlow's theory, the thin-wall approximation applies and the stress components given in Eq. (19) agree with Eq. (20). Tangential tensile stress of 400 MPa and hydrostatic stress of 200 MPa occur. The positive hydrostatic stress $\sigma_H = p_G r/2t$, which influences the stress-enhanced hydrogen solubility, is almost constant throughout the pipe wall. Fig. 4b shows the dependency of the multiaxial stress occurring in the pipe wall from internal gas pressure. According to Barlow's equations, each stress component increases linearly with increasing p_G . Basic design criteria require that the equivalent stress σ_{eq} is smaller than the yield strength $R_{p0.2}$ to avoid any plastic deformation. In Fig. 4b σ_{eq} according to von Mises increases linearly as function of p_G and reaches 400 MPa and 700 MPa at gas pressures of 100 bar and 200 bar, respectively. $\sigma_{eq} = 700$ MPa exceeds $R_{p0.2}$ of commercial carbon steels. σ_H reaches 200 MPa at 100 bar and 400 MPa at 200 bar. Note that $\sigma_H = \sigma_t/2$. According to Eq. (19), increasing the wall thickness t decreases the stresses at the given gas pressure of $p_G = 100$ bar and for the given inner radius of $r_1 = 200$ mm, as shown in Fig. 5a. Tangential stress and axial stress are tensile throughout the wall and they decrease steadily with increasing wall thickness. The radial stress of -10 MPa is negative (compression stress) and does not change with increasing wall thickness. Thus, the hydrostatic stress decreases significantly from 99 MPa to 5 MPa if the wall thickness increases from 10 mm to 200 mm.

For thick-walled pressure vessels with the ratio of $r_a/r_1 = 2$, the tangential stress at the inner surface radius is $\sigma_t = 5p_G/3$, as indicated in Fig. 5a. At higher pressures the radial stress cannot be neglected, and it is equal to the negative gas pressure at the inner radius, $\sigma_r = -p_G$. The radial stress decreases linearly through the wall and becomes zero at the outer radius r_a . As shown in Fig. 5b, the stresses in thick-walled pressure vessels increase linearly with increasing inner gas pressure.

Table 1 – Multiaxial stress states in bulk specimens exposed to an environmental gas pressure p_G and cylindrical stress components [47].

No.	Short description	Stress state	Schematic of the problem
Ref.	Bulky specimen (Reference state)	$\sigma_H = 0$	
1	Externally pressurized bulky specimen	$\sigma_r = -p_G$ $\sigma_t = -p_G$ $\sigma_a = -p_G$ $\sigma_H = -p_G$ $\sigma_{eq} = 0$	
2	Internally pressurized thin-walled pipe (Barlow's formula for pipes with $t \ll r_0$)	$\sigma_r = 0$ $\sigma_t = \frac{p_G r_i}{t}$ $\sigma_a = \frac{p_G r_i}{2t}$ $\sigma_H = \frac{p_G r_i}{2t}$ $\sigma_{eq} = \frac{\sqrt{3} p_G r_i}{2t}$	
3	Internally pressurized thick-walled vessel with $\frac{r_a}{r_i} = 2$	$\sigma_r(r_i) = -p_G$ $\sigma_t(r_i) = \frac{5p_G}{3}$ $\sigma_a(r_i) = \frac{p_G r_i}{2t}$ $\sigma_H = \frac{p_G}{3} \left(\frac{2}{3} + \frac{r_i}{2t} \right)$	

For $r_i = 200$ mm and $t = 200$ mm, σ_{eq} according to von Mises is less than 300 MPa and $\sigma_H = 50$ MPa even at $p_G = 1000$ bar.

Experimental procedure

Cylindrical specimens with diameter of 3 mm and height of 15 mm were machined out of a L450 pipe steel. Before the specimens were placed inside of an autoclave, their surfaces

were grinded, polished and rinsed with acetone. High-pressure charging was applied at 200 bar and 80 °C as well as at 1000 bar and 50 °C. The duration of hydrogen gas charging was 3 weeks. When the specimens were removed from the autoclave, they were stored directly inside of a liquid nitrogen bath to suppress any hydrogen diffusion. For the quantification of the hydrogen content, a Bruker G8 Galileo coupled with an infrared furnace and with a mass spectrometer was used, as described in Ref. [49]. The specimens were

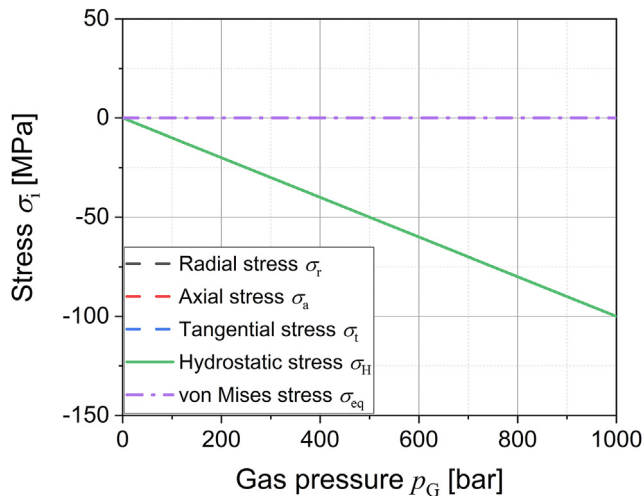


Fig. 3 – Multi-axial stress state in bulky specimens exposed to an external gas pressure on laboratory scale.

thawed in acetone for 20 s before there were dried using inert nitrogen gas. Afterwards the samples were directly put into the infrared furnace and they were immediately heated up to 400 °C.

Results and discussion

Parameter identification

For calculating the hydrogen solubility c_H of a given material as function of total gas pressure p_G , temperature T and applied hydrostatic stress σ_H , a set of four constant parameters needs to be identified, namely.

1. The solubility coefficient K_0 ,
2. The solution enthalpy ΔH_s ,
3. The partial molar volume V_H ,
4. And the van der Waals constant b .

As shown in Fig. 6a, K_0 was measured for different materials [50–53]. Smaller values ranging from 1.7 to 33 wppm/bar^{0.5} were determined by different authors [50–52] using a permeation setup at temperatures above 100 °C, which allows recording the transient increase of the pressure as function of time. Disc-shaped specimens were used to separate a pressurized charging cell from an evacuated measurement cell equipped with a mass spectrometer. The applied pressure was very low, but it was even increased to 30 bar. At temperatures above 100 °C hydrogen trapping in bulky ferrite is de facto thermally suppressed, and lattice-controlled diffusion can be assumed [55]. Once all trapping sites are thermally activated, the equilibrium coefficient $K = \phi/D_{\text{eff}}$, where ϕ is the permeability coefficient and D_{eff} is the effective diffusivity. However, at lower temperature hydrogen diffusion is bulk-controlled [55,56] rather than lattice-controlled, and trapping sites in the microstructure retard long-range chemical diffusion [16,31,55,57]. Since the chemical diffusivity D_{chem} is not independent from the pressure [16,58], the equilibrium coefficient will be significantly affected by the specific method of determination. More recent approaches enable measuring the solubility coefficient directly by reliable autoclave charging techniques at low temperatures combined with subsequent thermal desorption analysis (TDA) [53,54,59–61] without any restriction to lattice-controlled diffusion. However, this technique has some crucial limitations, such as increase of diffusion coefficients at elevated temperatures and relatively long time needed for opening the pressurized autoclaves. Especially at higher temperatures the hydrogen content in bulky specimens can easily follow the pressure drop during evacuation, which may lead to an underestimation of the hydrogen solubility. A solubility coefficient of about 300 wppmbar^{-0.5} was evaluated from the measured data at 80 °C provided by Trautmann et al. [53,54]. They used autoclaves to charge cuboid specimens with pure hydrogen gas before measuring their hydrogen contents using TDA at 950 °C. The difference in the solubility coefficient K_0 by using the two different methods may be due to the difference of the applied temperatures. In Fig. 6b calculated solubility coefficients according to Eq. (17) were plotted as function of temperature, binding energy and trap density. Trap densities between 10⁻⁹ and 10⁻⁷ mol/mm³

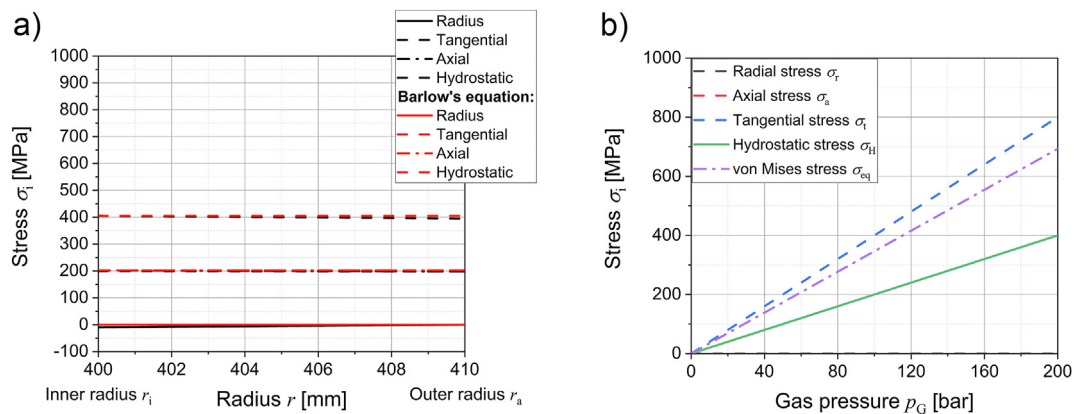


Fig. 4 – Multi-axial stresses in a thin-walled pipe a) as function of the radius at given gas pressure of 100 bar and b) as function of internal gas pressure for the inner surface radius $r_i = 400$ mm and the wall thickness $t = 10$ mm.

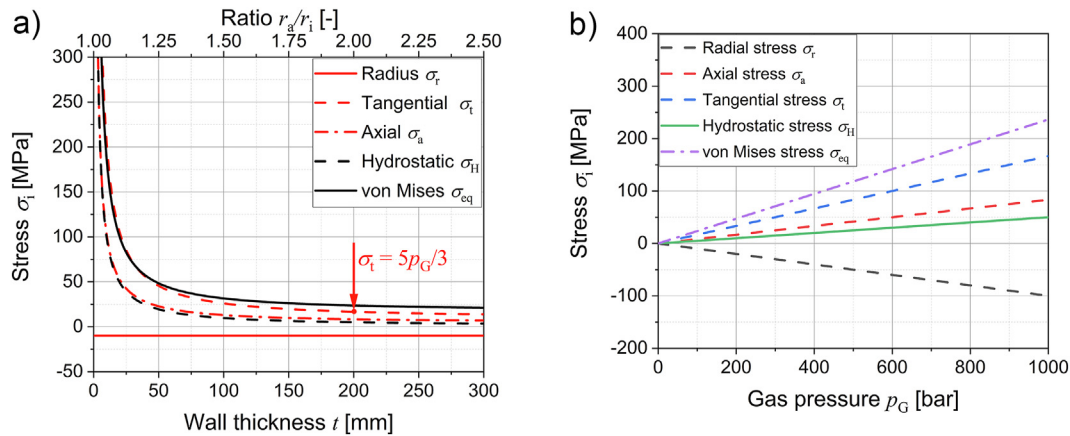


Fig. 5 – Stress state in a thick-walled pressure vessel a) as function of the wall thickness at given internal gas pressure of 100 bar and b) as function of gas pressure for the radius ratio of $r_a/r_i = 2$.

represent hydrogen trapping in cold rolled ferritic iron [31] or in dual phase steel [16]. The higher the binding energy and the higher the trap density, the higher is the hydrogen solubility coefficient which is in the range of 10^2 - 10^4 wppm/bar $^{0.5}$ at ambient temperature. With increasing temperatures trapping sites get thermally activated and the solubility coefficient decreases steadily. Once all trapping sites are fully activated, diffusion in the specimens is lattice-controlled and the solubility coefficient reaches a minimum. In the present work the minimum was 10 wppm/bar $^{0.5}$, which is in good agreement with the results of permeation measurements [51,52]. Nevertheless, further experimental studies are necessary to clarify the role of trapping sites on the equilibrium coefficient. A combination of both techniques would be beneficial for compensating the limitations caused by high temperatures and high gas pressures.

As shown in Fig. 7a, the solution enthalpy ΔH_s of ferritic iron was well studied in literature [50–52,62,64] and a value of 27 kJ/mol was chosen in the present work. This value agrees with data published by Nelson and Stein [52], who measured the solution enthalpy of different heat-treated 4130 steels. Only Gadgeel and Johnson [51] found even lower values of 19–25 kJ/mol for different carbon steels. Although Trautmann et al. [53] published hydrogen solubilities of carbon steels only

for 25 °C and 80 °C, a rough estimation using Eq. (1) gives solution enthalpies less than 15 kJ/mol (red points in Fig. 7b). Depending on the temperature range and thus on the measurement technique the determined solution enthalpies can differ significantly. Therefore, the temperature dependency of the hydrogen solubility according to Eq. (17) was plotted in Fig. 7b. While the solution enthalpy is typically measured in the lattice diffusion-controlled temperature regime ($\gg 100$ °C) to be around 27 kJ/mol, at low temperatures the thermal activation of trapping sites at low temperatures can affect the evaluation significantly. ΔH_s decreases with decreasing temperature and can also change from negative (endothermic absorption) to positive at temperatures below zero. In other words, the gaseous hydrogen solubility can increase with decreasing temperature below a critical temperature of around -30 °C. Since this behavior is rather attributed to the increase of trapped hydrogen concentration c_T than to the change of ΔH_s , it is named “quasi-exothermic” absorption in the present work. Further measurements for validating the increase of the hydrogen solubility with decreasing temperature are necessary in the low temperature regime.

Dissolved hydrogen causes a lattice expansion in ferritic steels [46], and the partial molar volume V_H can directly be obtained from dilatation measurements. Fig. 8a shows

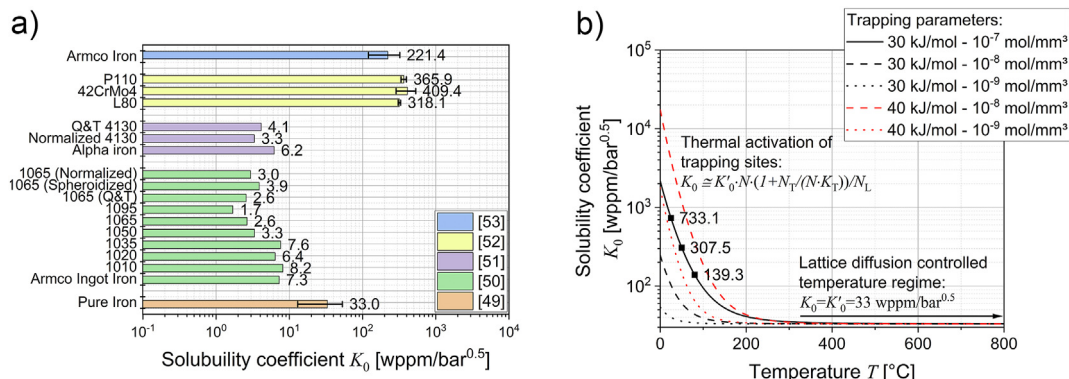


Fig. 6 – a) Measured solubility coefficients published in literature [50–54]. b) Temperature dependency of the hydrogen solubility as function of microstructural trapping sites.

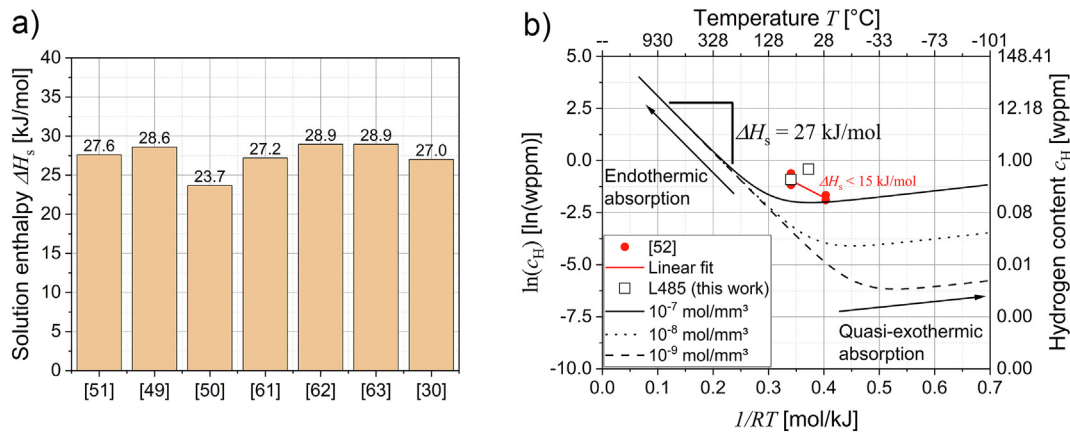


Fig. 7 – a) Measured solution enthalpies published in literature [30,50–52,62–64]. b) Temperature dependency of the hydrogen solubility considering the effect of microstructural trapping sites with the binding energy of 30 kJ/mol [53].

measured values of V_H of iron and steels in the range of 1220–3000 mm³/mol published in literature [26,63,65–67]. This corresponds approximately to the dilation of $\Delta l \approx 0.1$ nm for each hydrogen atom. According to Wipf [30] or Nagumo [9] the dilation per atom is similar for many metals and seems to be insensitive to temperature and microstructure [9,26,30]. Wagenblast and Wriedt determined $V_H = 2000$ mm³/mol [65], and they measured the dilation of iron wires at hydrogen partial pressures of about 0.02–0.97 bar and at high temperatures of 450–800 °C. For low-temperature and high-pressure applications the partial pressure p_{H_2} of the ideal gas needs to be replaced by the fugacity f , as given in Eq. (10). Numerous models and empirical relationships accounting for the real behavior of hydrogen gas by considering intermolecular van der Waals forces and the finite volume of hydrogen molecules exist [25,69–72]. The fugacity calculated using some of these models are plotted in Fig. 8b. Since $f \approx p_{H_2}$ for pressures up to 150 bar and at ambient temperatures, the ideal gas behavior can be assumed with reasonable accuracy. Extrapolating the fugacity up to 1000 bar shows large difference from the ideal gas behavior. For example, San Marchi et al. [25] fitted the van der Waals constant b to hydrogen data provided by Michels

et al. [73] from ambient temperature to 150 °C and for pressures up to 3000 bar, and they confirmed that $b \approx 15.84 \cdot 10^{-3}$ mm³/mol. Thus, f increases exponentially to 1984 bar, whereas p_{H_2} increases linearly to only 1000 bar ($f \approx 2p_{H_2}$). Krom and Bakker [69] suggested another relationship for describing the real behavior of hydrogen gas by calculating f . As shown in Fig. 8b, the obtained curves were quite similar. The constant, pressure- and temperature-independent parameters used for calculating the stress-enhanced hydrogen solubility in pressurized specimens, pipes and pressure vessels are summarized in Table 2. Since these parameters were not fitted to any specific material or hydrogen solubility measurement, they can be considered as rough estimation for ferritic and martensitic steels. The temperature dependency of the solubility coefficient is approximated by a single trap approach according to Eq. (9) with the binding energy of 30 kJ/mol and the trap density of 10^{-7} mol/mm³. This corresponds to the trapping capacity of highly deformed ferritic iron [31] or of ferritic-martensitic steels [15,16]. The solubility coefficient $K_0 = K'_0$ in the lattice diffusion-controlled regime at high temperatures was assumed as constant and corresponded to measurements of Quick and Johnson [50] for pure iron.

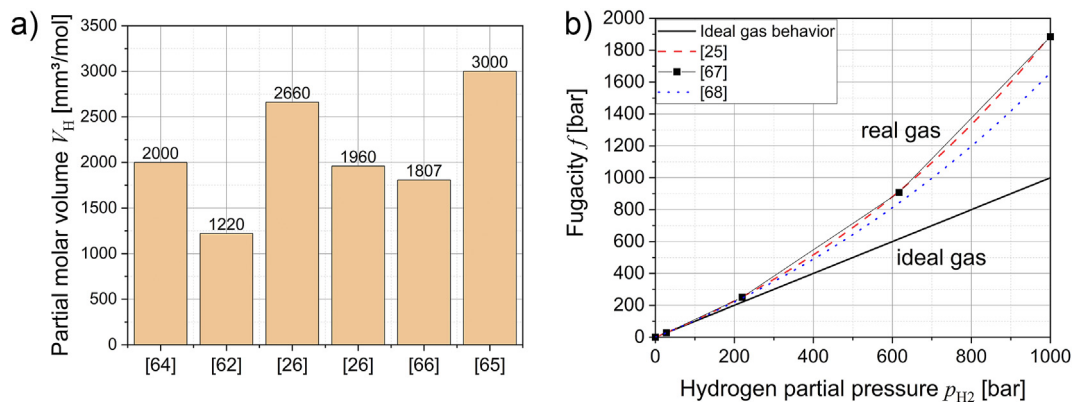


Fig. 8 – a) Published partial molar volume of hydrogen in ferritic iron [26,63,65–67]. b) Fugacity of real hydrogen gas at 25 °C as function of hydrogen partial pressure [25,68,69].

Table 2 – Parameters used for calculating the stress-enhanced hydrogen solubility.

Parameter	Symbol	Value	Unit	Reference(s)
Binding energy	E_b	30	kJ/mol	Assumption made in this work based on [16,74]
Constant pre-factor	K'_0	33	wppm/bar ^{0.5}	[50]
Density of interstitial lattice sites	N_L	$8.5 \cdot 10^{-4}$	mol/mm ³	[75]
Partial molar volume	V_H	2000	mm ³ /mol	[65]
Solution enthalpy	ΔH_s	27	kJ/mol	[30]
Trap density	N_T	10^{-7}	mol/mm ³	Assumption made in this work based on [16]
Van der Waals constant	b	$15.84 \cdot 10^3$	mm ³ /mol	[25]

Individual values of the solubility coefficient are plotted for 25 °C, 50 °C and 80 °C in Fig. 6b.

Externally pressurized bulky specimens

For characterizing the hydrogen solubility of materials, often cylindrical or cuboidal specimens are charged with gaseous hydrogen under compressive conditions. Lack of knowledge exists about the hydrogen solubility of ferritic or martensitic steels at low temperatures and high hydrogen gas pressures. Therefore, the present work compares analytical predictions with measured hydrogen solubilities of ferritic-pearlitic L450 steel and other commercial carbon steels published by Trautmann et al. [53]. As shown in Fig. 9, the analytical

predictions are in reasonable agreement with the measurements even at total gas pressures of 1000 bar. The difference of calculated and measured hydrogen solubilities is about ± 0.1 wppm at 25 °C and 50 °C, as shown in Fig. 9a and b, respectively, and thus comparable with the accuracy of state-of-the-art hydrogen extraction techniques. As shown in Fig. 9c, the calculations underestimate the solubility at 80 °C. This is most likely related to the temperature dependency of the solubility coefficient rather than to the measured solution enthalpy. Hydrogen trapping in commercial steels is very complex, especially in the presence of carbides [28,35], and requires a multiple trap approach rather than an effective single trap approach (Table 2) to capture the temperature dependency of the solubility coefficient more accurately. Temperature-

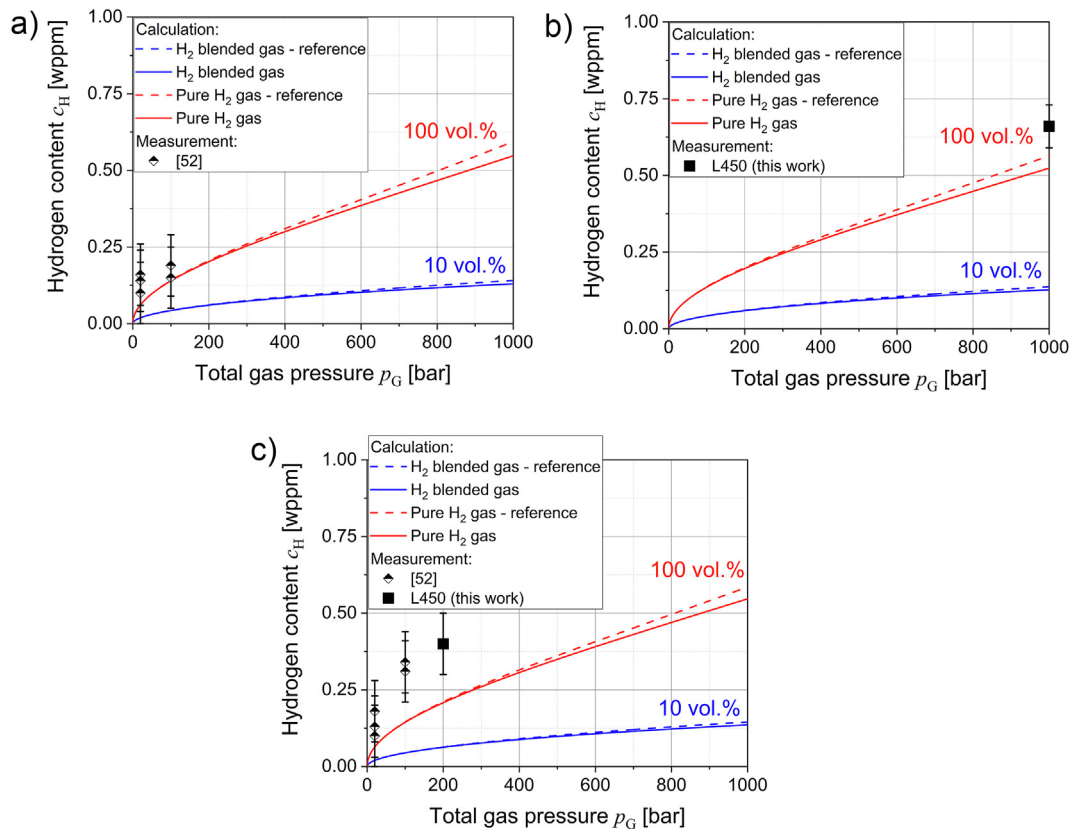


Fig. 9 – Hydrogen solubility of externally pressurized bulky specimens as function of total gas pressure and temperature: a) 25 °C, b) 50 °C and c) 80 °C [53].

Table 3 – Influence of component geometry and pure hydrogen gas pressure on the calculated hydrogen solubility at 25 °C.

Gas pressure p_G [bar]	Hydrogen solubility c_H [wppm]		
	Bulky specimen	Thin-walled pipe	Thick-walled pressure vessel
70 (MOP)	0.12	0.13	0.12
200	0.20	0.28	0.21
500	0.34		0.36
700	0.43		0.46
1000	0.55		0.61

dependent parametrization of the solubility coefficient would open the possibility for comparing electrochemical and gaseous hydrogen uptake by evaluating trapping sites using (i) Kissinger's theory [55,56] and/or (ii) recorded thermal desorption spectra measured after electrochemical charging [28,35,55]. As shown in Fig. 9a, the hydrogen solubility increases with the square root of the external total gas pressure at 25 °C and strongly depends on the hydrogen partial pressure. While the hydrogen content of 10% in a hydrogen blended gas causes a hydrogen solubility of 0.13 wppm at 1000 bar, pure hydrogen gas increases the hydrogen solubility to 0.55 wppm. Nevertheless, if the total gas pressure is limited to 200 bar the hydrogen solubility of bulky specimens stays below 0.2 wppm, as summarized in Table 3. The present calculations also consider the effect of compressive stresses acting on the specimens by the outer total gas pressure. Compressive stresses reduce the hydrogen solubility by increasing the effective solution enthalpy $\Delta H_s - \sigma_H V_H$. However, as shown in Fig. 9 this effect is negligible even at gas pressures of 1000 bar, as the difference in the hydrogen solubility (compared with the reference without considering the stress effect) is less than 0.05 wppm. This is less than the detection limit of most hydrogen measuring devices.

Hydrogen solubility of internally pressurized pipes and vessels

The hydrogen solubility c_H of internally pressurized pipelines or pressure vessels can differ from the laboratory test results

by the effect of stress-enhanced hydrogen uptake. The internally applied total gas pressure causes tensile stresses at the inner surface radius r_i of the pipes which decrease the effective solution enthalpy $\Delta H_s - \sigma_H V_H$. The magnitude of the hydrostatic stress σ_H depends only on the dimensions of the pipe and of the internal total gas pressure, as described in section 2.4. Note that macroscopic residual stresses resulting from, e.g., thermomechanical treatments [76], are not considered in the present work. In Fig. 10a the hydrogen solubility in thin-walled pipes is plotted as function of the total gas pressure. In general, the hydrogen solubility in pipes increases with the total gas pressure and it also increases with the hydrogen content in the gas mixture. For both conditions, namely hydrogen blended gas and pure hydrogen gas, the hydrogen solubility in the pipes shows a slight underestimation compared to the experimentally hydrogen solubility, which is determined under hydrostatic compression. Therefore, the experimental hydrogen solubility is indicated as "autoclave" in Fig. 10. The difference increases with the total gas pressure. The maximum difference was observed for pure hydrogen gas. As summarized in Table 3, the hydrogen solubility increased by 0.01 wppm at the gas pressure of 70 bar, and by 0.08 wppm at 200 bar compared to the externally pressurized bulky specimens. In Fig. 10b, the hydrogen solubility of thick-walled pressure vessels is illustrated as function of the total gas pressure, and characteristic values are summarized in Table 3. They range from 0.12 wppm at 70 bar to 0.61 wppm at 1000 bar. Due to the higher radius ratio of $r_a/r_i = 2$, the hydrostatic stress caused by the internal total gas pressure was much smaller than in thin-walled pipes. Hence, the effect of stress-enhanced hydrogen uptake in thick-walled pressure vessels was only minor with less than 0.06 wppm even at highest pure gas pressures of 1000 bar. Pipelines or pressure vessels enable distribution of hydrogen gas over long distances. Pipelines usually operate at low pressures with a maximum operating pressure (MOP) of 70 bar. According to the present calculations, this corresponds to a hydrogen solubility of around 0.1 wppm. Increasing the gas pressure in future gas grids could be necessary for compensating the lower volumetric energy density of hydrogen gas compared to natural gas. Therefore, the calculated hydrogen solubility in pipeline materials was plotted in Fig. 10a up to the gas

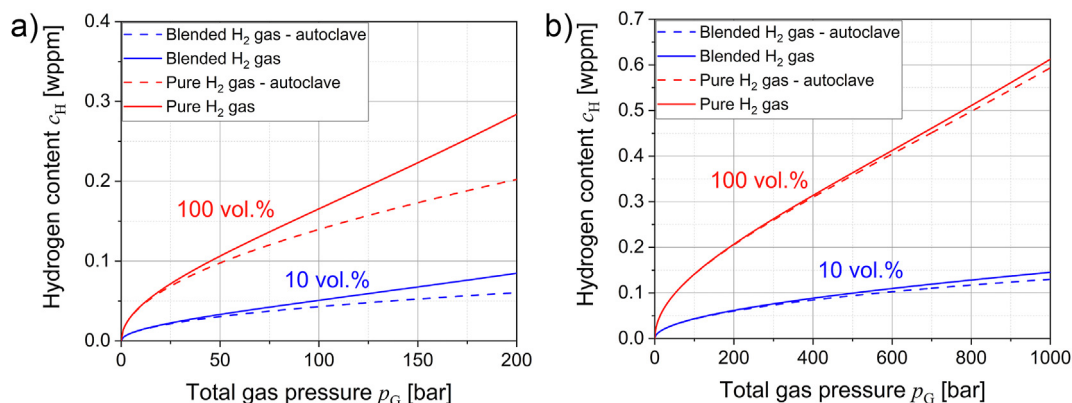


Fig. 10 – : Calculated hydrogen solubility of internally pressurized a) thin-walled pipes and b) thick-walled pressure vessels at 25 °C.

pressure of 200 bar. Even higher pressures can be applied in pressure vessels to increase the amount of stored hydrogen gas, which also increases the hydrogen solubility, as shown in Fig. 10b. Based on the present calculations, the hydrogen contents absorbed during service of pipelines and pressure vessels do not seem to be negligible. However, the contents are acceptable with respect to HE, if the mechanical strength of the pipe materials is low. This would limit stress-enhanced hydrogen uptake and increase the HE resistivity. Although results of the laboratory tests underestimate slightly the hydrogen solubility in pipelines and pressure vessels, the effect of stress-enhanced hydrogen solubility is negligible if the surfaces are smooth. This is also in agreement with the predictions of Wipf [30], who argued that the gain in solution energy is negligible in most calculations. However, hydrostatic stresses are strongly intensified at micro-notches or at crack tips. There the hydrostatic stresses can reach several Gigapascal, which needs further detailed investigations [38].

Conclusions

This work calculated and measured the hydrogen solubility in ferritic steel components at high gas pressures up to 1000 bar and at temperatures from -100 to 900 °C. The following conclusions can be drawn from the present work:

- a new thermodynamic relationship was proposed, which extends Sievert's law to low temperatures and high gas pressures considering microstructural trapping sites, fugacity and multiaxial stress states as following

$$c_H = K_0(T) \sqrt{f} \exp\left(-\frac{\Delta H_s - \sigma_H V_H}{RT}\right)$$

- This equation was parametrized using a set of four constant parameters. Two of them, namely the solution enthalpy and the partial molar volume of hydrogen in steels, are similar for iron and many steels and independent of temperature and microstructure.
- Challenges in the parametrization of Sievert's law at low temperatures and high gas pressures were identified using the new equation. In particular, the solution enthalpy should be determined at high temperatures, while the solubility coefficient needs to be measured over a wide range of temperature using a combination of ex-situ and in-situ techniques.
- The parametrized equation was validated using measured hydrogen contents at 200 and 1000 bar. The accuracy of the calculated hydrogen contents was in the range of ± 0.1 wppm.
- Measured and calculated hydrogen contents in pipes and pressure vessels up to 0.3 wppm at 200 bar and 0.6 wppm at 1000 bar are not negligible and need careful examination with respect to hydrogen embrittlement.

Future work should focus on the stress-enhanced hydrogen solubility at micro-notches and on the role of

compressive residual stresses as mitigation strategy against hydrogen embrittlement.

Declaration of competing interest

The authors declare that they have no known competing financial interests or personal relationships that could have appeared to influence the work reported in this paper.

Nomenclature

b	van der Waals constant [mm^3/mol]
c	Total molar hydrogen concentration [mol/mm^3]
c_H	Hydrogen solubility [wppm]
$c_{H,0}$	Hydrogen solubility in unstressed state [wppm]
c_L	Lattice concentration [mol/mm^3]
c_T	Trap concentration [mol/mm^3]
D_{eff}	Effective diffusivity [mm^2/s]
D_{chem}	Chemical diffusion coefficient [mm^2/s]
ΔH_s	Solution enthalpy [kJ/mol]
ΔS	Changes in entropy [kJ/molK]
E	Young's modulus [MPa]
E_b	Binding energy [kJ/mol]
f	Fugacity [bar]
γ	Fugacity coefficient [bar]
H_L	Lattice hydrogen atom
H_T	Trapped hydrogen atom
H_2	Hydrogen gas molecule
K	Equilibrium coefficient [wppmbar $^{-0.5}$]
K_0	Solubility coefficient [wppmbar $^{-0.5}$]
K'_0	Constant pre-factor [wppmbar $^{-0.5}$]
K_T	Equilibrium constant [-]
M	Molar mass of hydrogen [g/mol]
μ_{H_2}	Generalized chemical potential of diatomic hydrogen molecules [kJ/mol]
$\mu_{H_2,0}$	Standard chemical potential of diatomic hydrogen molecules [kJ/mol]
μ_L	Generalized chemical potential of lattice hydrogen [kJ/mol]
$\mu_{L,0}$	Standard chemical potential of lattice hydrogen atoms [kJ/mol]
N	Total density of possible hydrogen sites [mol/mm^3]
N_L	Density of interstitial lattice sites [mol/mm^3]
N_T	Trap density [mol/mm^3]
p_G	Total gas pressure [bar]
p_{H_2}	Hydrogen partial pressure [bar]
R	Universal gas constant [kJ/molK]
$R_{p0.2}$	Yield strength [MPa]
r	Radius [mm]
r_a	Outer surface radius of the tube [mm]
r_i	Inner surface radius of the tube [mm]
r_0	Average tube radius [mm]
ρ	Density of steel [g/mm^3]
σ_a	Axial stress [MPa]
σ_{eq}	Equivalent stress according to von Mises [MPa]
σ_H	Hydrostatic stress [MPa]
σ_i	Principal stress in direction i [MPa]
σ_{ij}	Stress tensor [MPa]
σ_r	Radial stress [MPa]

σ_t	Tangential stress [MPa]
σ_y	Yield stress [MPa]
σ_1	Uniaxial tensile stress [MPa]
T	Temperature [K]
t	Thickness of the tube wall [mm]
V_H	Partial molar volume [mm ³ /mol]
V_L	Vacant interstitial lattice site
V_T	Vacant trapping site
ϕ	Permeability coefficient [mol/mmbar ^{0.5} s]
y_L	Lattice site fraction [–]
y_T	Trap site fraction [–]

REFERENCES

- [1] COM, The European Green Deal. Eur Community 2019;53:24. <https://eur-lex.europa.eu/legal-content/EN/TXT/PDF/?uri=CELEX:52019DC0640&from=EN>.
- [2] Bossel U, Eliasson B. Energy and hydrogen economy. Eur. Fuel Cell Forum, Lucerne.; 2002. p. 36.
- [3] Dodds PE, Demoullin S. Conversion of the UK gas system to transport hydrogen. Int J Hydrogen Energy 2013;38:7189–200. <https://doi.org/10.1016/j.ijhydene.2013.03.070>.
- [4] Sims JR. Standards and codes to control hydrogen-induced cracking in pressure vessels and pipes for hydrogen gas storage and transport, Gaseous Hydrog. Embrittlement Mater. Energy Technol. Probl. Its Characterisation Eff. Part. Alloy Classes 2012;177–92. <https://doi.org/10.1533/9780857093899.1.177>.
- [5] A.S. Tazedakis, N. Voudouris, E. Dourdounis, G. Mannucci, L.F. Di Vito, A.F. Corinth, P. Sa, Qualification of high-strength Linepipes for hydrogen Transportation based on ASME B31.12 Code, [n.d.].
- [6] Depover T, Pérez Escobar D, Wallaert E, Zermout Z, Verbeken K. Effect of hydrogen charging on the mechanical properties of advanced high strength steels. Int J Hydrogen Energy 2014;39:4647–56. <https://doi.org/10.1016/j.ijhydene.2013.12.190>.
- [7] Lynch S. Discussion of some recent literature on hydrogen-embrittlement mechanisms: addressing common misunderstandings. Corrosion Rev 2019;37:377–95. <https://doi.org/10.1515/corrrev-2019-0017>.
- [8] Lynch SP. Progress towards understanding mechanisms of hydrogen embrittlement and stress corrosion cracking. NACE - Int. Corros. Conf. Ser. 2007:74931–749355.
- [9] Nagumo M. Fundamentals of hydrogen embrittlement. Singapore: Springer Singapore; 2016. <https://doi.org/10.1007/978-981-10-0161-1>.
- [10] Johnson WH. On some remarkable changes produced in iron and steel by the action of hydrogen and acids. Nature 1875;11:393. <https://doi.org/10.1038/011393a0>.
- [11] Djukic MB, Sijacki Zeravcic V, Bakic GM, Sedmak A, Rajcic B. Hydrogen damage of steels: a case study and hydrogen embrittlement model. Eng Fail Anal 2015;58:485–98. <https://doi.org/10.1016/j.engfailanal.2015.05.017>.
- [12] Lynch SP. Environmentally assisted cracking: overview of evidence for an adsorption-induced localised-slip process. Acta Metall 1988;36:2639–61. [https://doi.org/10.1016/0001-6160\(88\)90113-7](https://doi.org/10.1016/0001-6160(88)90113-7).
- [13] Nagumo M. Hydrogen related failure of steels - a new aspect. Mater Sci Technol 2004;20:940–50. <https://doi.org/10.1179/026708304225019687>.
- [14] Kirchheim R. Revisiting hydrogen embrittlement models and hydrogen-induced homogeneous nucleation of dislocations. Scripta Mater 2010;62:67–70. <https://doi.org/10.1016/j.scriptamat.2009.09.037>.
- [15] Drexler A, Helic B, Silvayeh Z, Sommitsch C, Mraczek K, Domitner J. Influence of plastic deformation on the hydrogen embrittlement susceptibility of dual phase steels. Key Eng Mater 2022;926:2077–91. <https://doi.org/10.4028/p-oeev61>.
- [16] Drexler A, Helic B, Silvayeh Z, Mraczek K, Sommitsch C, Domitner J. The role of hydrogen diffusion, trapping and desorption in dual phase steels. J Mater Sci 2022;57:4789–805. <https://doi.org/10.1007/s10853-021-06830-0>.
- [17] Beachem CD. A new model for hydrogen-assisted cracking (hydrogen “embrittlement”). Metall Mater Trans B 1972;3:441–55. <https://doi.org/10.1007/BF02642048>.
- [18] Drexler A, Bergmann C, Manke G, Kokotin V, Mraczek K, Pohl M, Ecker W. On the local evaluation of the hydrogen susceptibility of cold-formed and heat treated advanced high strength steel (AHSS) sheets. Mater Sci Eng 2021;800:140276. <https://doi.org/10.1016/j.msea.2020.140276>.
- [19] Drexler A, Ecker W, Winzer N, Mraczek K, Kokotin V, Manke G, Bergmann C. A step towards numerical evaluation of the local hydrogen susceptibility of punched and cold-formed advanced high strength steel (AHSS) sheets. In: Duprez L, editor. SteelyHydrogen, ocas; 2018. A02. <http://steelyhydrogen2018proc.be/articles/pdf/2>.
- [20] Nöger D. Interaction of the H₂ molecule with carbon nanostructures : a DFT study. Montanuniversität Leoben; 2018.
- [21] Klüpfel S, Klüpfel P, Jónsson H. The effect of the Perdew-Zunger self-interaction correction to density functionals on the energetics of small molecules. J Chem Phys 2012;137:124102. <https://doi.org/10.1063/1.4752229>.
- [22] Sieverts A. Palladium und Wasserstoff. I. Z Phys Chem 1914;88U:103–27. <https://doi.org/10.1515/zpch-1914-8811>.
- [23] Sieverts A. Palladium und Wasserstoff. II. Z Phys Chem 1914;88U:451–78. <https://doi.org/10.1515/zpch-1914-8832>.
- [24] Nagumo M. Function of hydrogen in embrittlement of high-strength steels. ISIJ Int 2001;41:590–8. <https://doi.org/10.2355/isijinternational.41.590>.
- [25] Marchi CS, Somerday BP, Robinson SL. Permeability, solubility and diffusivity of hydrogen isotopes in stainless steels at high gas pressures. Int J Hydrogen Energy 2007;32:100–16. <https://doi.org/10.1016/j.ijhydene.2006.05.008>.
- [26] Bockris JOM, Subramanyan PK. A thermodynamic analysis of hydrogen in metals in the presence of an applied stress field. Acta Metall 1971;19:1205–8. [https://doi.org/10.1016/0001-6160\(71\)90053-8](https://doi.org/10.1016/0001-6160(71)90053-8).
- [27] Wriedt HA, Oriani RA. Effect of tensile and compressive elastic stress on equilibrium hydrogen solubility in a solid. Acta Metall 1970;18:753–60. [https://doi.org/10.1016/0001-6160\(70\)90039-8](https://doi.org/10.1016/0001-6160(70)90039-8).
- [28] Drexler A, Depover T, Leitner S, Verbeken K, Ecker W. Microstructural based hydrogen diffusion and trapping models applied to Fe–C X alloys. J Alloys Compd 2020;826:154057. <https://doi.org/10.1016/j.jallcom.2020.154057>.
- [29] Kholobina AS, Pippin R, Romaner L, Scheiber D, Ecker W, Razumovskiy VI. Hydrogen trapping in bcc iron. Materials 2020;13:2288. <https://doi.org/10.3390/ma13102288>.
- [30] Wipf H. Solubility and diffusion of hydrogen in pure metals and alloys. Phys Scripta 2001;T94:43. <https://doi.org/10.1238/Physica.Topical.094a00043>.
- [31] Drexler A, Siegl W, Ecker W, Tkadletz M, Klösch G, Schnideritsch H, Mori G, Svoboda J, Fischer FD. Cycled hydrogen permeation through Armco iron – a joint experimental and modeling approach. Corrosion Sci 2020;176:109017. <https://doi.org/10.1016/j.corsci.2020.109017>.
- [32] Siegl W, Ecker W, Klarner J, Kloesch G, Mori G, Drexler A, Winter G, Schnideritsch H. Hydrogen trapping in heat treated

- and deformed Armco iron. In: *Nace - int. Corros. Conf. Ser.*; 2019. p. 1–12.
- [33] Oriani RA. The diffusion and trapping of hydrogen in steel. *Acta Metall* 1970;18:147–57. [https://doi.org/10.1016/0001-6160\(70\)90078-7](https://doi.org/10.1016/0001-6160(70)90078-7).
- [34] Oriani RA. A mechanistic theory of hydrogen embrittlement of steels. *Berichte Der Bunsengesellschaft Für Phys. Chemie.* 1972;76:848–57. <https://doi.org/10.1002/BBPC.19720760864>.
- [35] Drexler A, Depover T, Verbeken K, Ecker W. Model-based interpretation of thermal desorption spectra of Fe-C-Ti alloys. *J Alloys Compd* 2019;789:647–57. <https://doi.org/10.1016/j.jallcom.2019.03.102>.
- [36] Rhode M, Mente T, Steppan E, Steger J, Kannengiesser T. Hydrogen trapping in T24 Cr-Mo-V steel weld joints—microstructure effect vs. experimental influence on activation energy for diffusion. *Weld World* 2018;62:277–87. <https://doi.org/10.1007/s40194-017-0546-6>.
- [37] Drexler A, Domitner J, Sommitsch C. Modeling of hydrogen diffusion in Slow Strain rate (SSR) testing of notched samples. 143rd ed. Springer Nature Switzerland AG; 2021. https://doi.org/10.1007/978-3-030-66948-5_6.
- [38] Drexler A, He S, Pippan R, Romaner L, Razumovskiy VI, Ecker W. Hydrogen segregation near a crack tip in nickel. *Scripta Mater* 2021;194:113697. <https://doi.org/10.1016/j.scriptamat.2020.113697>.
- [39] Kloos KH. Eigenspannungen, Definition und Entstehungsursachen, *Materwiss. Werksttech* 1979;10:293–302. <https://doi.org/10.1002/mawe.19790100906>.
- [40] Kan B, Yang ZX, Wang Z, Li JX, Zhou QJ, Su YJ, Qiao LJ, Volinsky AA. Hydrogen redistribution under stress-induced diffusion and corresponding fracture behaviour of a structural steel. *Mater Sci Technol* 2017;33:1539–47. <https://doi.org/10.1080/02670836.2017.1325562>.
- [41] Hussein A, Krom AHM, Dey P, Sunnardianto GK, Moulto OA, Walters CL. The effect of hydrogen content and yield strength on the distribution of hydrogen in steel: a diffusion coupled micromechanical FEM study. *Acta Mater* 2021;209:116799. <https://doi.org/10.1016/j.actamat.2021.116799>.
- [42] Svoboda J, Fischer FD. Modelling for hydrogen diffusion in metals with traps revisited. *Acta Mater* 2012;60:1211–20. <https://doi.org/10.1016/j.actamat.2011.11.025>.
- [43] Kirchheim R. Solubility, diffusivity and trapping of hydrogen in dilute alloys. Deformed and amorphous metals—II. *Acta Metall* 1982;30:1069–78. [https://doi.org/10.1016/0001-6160\(82\)90003-7](https://doi.org/10.1016/0001-6160(82)90003-7).
- [44] Svoboda J, Fischer FD, Fratzl P. Diffusion and creep in multi-component alloys with non-ideal sources and sinks for vacancies. *Acta Mater* 2006;54:3043–53. <https://doi.org/10.1016/j.actamat.2006.02.041>.
- [45] Drexler A, He S, Razumovskiy V, Romaner L, Ecker W, Pippan R. Verification of the generalised chemical potential for stress-driven hydrogen diffusion in nickel. *Phil Mag Lett* 2020;100:513–23. <https://doi.org/10.1080/09500839.2020.1808253>.
- [46] Svoboda J, Ecker W, Razumovskiy VI, Zickler GA, Fischer FD. Kinetics of interaction of impurity interstitials with dislocations revisited. *Prog Mater Sci* 2019;101:172–206. <https://doi.org/10.1016/j.pmatsci.2018.10.001>.
- [47] Mang G, Hofstetter H. *Festigkeitslehre*. 5th ed. Springer Vieweg; 2018. <https://doi.org/10.1007/978-3-662-57564-2>.
- [48] Drexler A, Estilaei H, Helic B, Mraczek K. Dependency of internal hydrogen embrittlement on the hydrogen distribution in industrial DP600 dual phase steel. In: *SteelyHydrogen*; 2022. p. 1–14. Ghent.
- [49] Rhode M, Schaupp T, Muenster C, Mente T, Boellinghaus T, Kannengiesser T. Hydrogen determination in welded specimens by carrier gas hot extraction—a review on the main parameters and their effects on hydrogen measurement. *Weld World* 2019;63:511–26. <https://doi.org/10.1007/s40194-018-0664-9>.
- [50] Quick NR, Johnson HH. Hydrogen and deuterium in iron, 49–506°C. *Acta Metall* 1978;26:903–7. [https://doi.org/10.1016/0001-6160\(78\)90041-X](https://doi.org/10.1016/0001-6160(78)90041-X).
- [51] Gadgeel VL, Johnson DL. Gas-phase hydrogen permeation and diffusion in carbon steels as a function of carbon content from 500 to 900 K. *J Mater Energy Syst* 1979;1:32–40. <https://doi.org/10.1007/BF02833976>.
- [52] Nelson HG, Stein JE. Gas-phase hydrogen permeation through alpha iron, 4130 steel, and 304 stainless steel from less than 100 C to near 600 °C. Washington, D.C. <http://hdl.handle.net/2060/19730012715>; 1973.
- [53] Trautmann A, Mori G, Oberndorfer M, Bauer S, Holzer C, Dittmann C. Hydrogen uptake and embrittlement of carbon steels in various environments. *Materials* 2020;13:1–16. <https://doi.org/10.3390/MA13163604>.
- [54] Truschner M, Trautmann A, Mori G. The basics of hydrogen uptake in iron and steel. *BHM Berg- Hüttenmännische Monatsh* 2021;166:443–9. <https://doi.org/10.1007/s00501-021-01142-x>.
- [55] Drexler A, Vandewalle L, Depover T, Verbeken K, Domitner J. Critical verification of the Kissinger theory to evaluate thermal desorption spectra. *Int J Hydrogen Energy* 2021;46:39590–606. <https://doi.org/10.1016/j.ijhydene.2021.09.171>.
- [56] Kirchheim R. Bulk diffusion-controlled thermal desorption spectroscopy with examples for hydrogen in iron. *Metall. Mater. Trans. A Phys. Metall. Mater. Sci.* 2016;47:672–96. <https://doi.org/10.1007/s11661-015-3236-2>.
- [57] Svoboda J, Mori G, Prethaler A, Fischer FD. Determination of trapping parameters and the chemical diffusion coefficient from hydrogen permeation experiments. *Corrosion Sci* 2014;82:93–100. <https://doi.org/10.1016/j.corsci.2014.01.002>.
- [58] Zafra A, Harris Z, Sun C, Martínez-Pañeda E. Comparison of hydrogen diffusivities measured by electrochemical permeation and temperature-programmed desorption in cold-rolled pure iron. *J Nat Gas Sci Eng* 2021;98:104365. <https://doi.org/10.1016/j.jngse.2021.104365>.
- [59] Zafra A, Álvarez G, Belzunce J, Rodríguez C. Influence of tempering time on the fracture toughness of hydrogen pre-charged 42CrMo4 steel. *Theor Appl Fract Mech* 2022;117. <https://doi.org/10.1016/j.tafmec.2021.103197>.
- [60] Zafra A, Peral LB, Belzunce J, Rodríguez C. Effect of hydrogen on the tensile properties of 42CrMo4 steel quenched and tempered at different temperatures. *Int J Hydrogen Energy* 2018;43:9068–82. <https://doi.org/10.1016/j.ijhydene.2018.03.158>.
- [61] Trautmann A, Mori G, Siegl W, Truschner M, Pfeiffer J, Kapp M, Keplinger A, Oberndorfer M, Bauer S. Hydrogen uptake of duplex 2205 at H₂ partial pressures UP to 100 bar, ESSC DUPLEX 2019 - 10th Eur. Stainl. In: *Steel Conf. - Sci. Mark.* 6th Eur. Duplex Stainl. Steel Conf. Exhib. 165; 2019. p. 338–45. <https://doi.org/10.1007/s00501-019-00934-6>.
- [62] Kumnick AJ, Johnson HH. Deep trapping states for hydrogen in deformed iron. *Acta Metall* 1980;28:33–9. [https://doi.org/10.1016/0001-6160\(80\)90038-3](https://doi.org/10.1016/0001-6160(80)90038-3).
- [63] Hirth JP. Effects of hydrogen on the properties of iron and steel. *Metall Trans A* 1980;11:861–90. <https://doi.org/10.1007/BF02654700>.
- [64] Christmann K. Interaction of hydrogen with solid surfaces. *Surf Sci Rep* 1988;9:1–163. [https://doi.org/10.1016/0167-5729\(88\)90009-X](https://doi.org/10.1016/0167-5729(88)90009-X).
- [65] Wagenblast H, Wriedt HA. Dilation of alpha iron by dissolved hydrogen at 450° to 800°C. *Metall Trans* 1971;2:1393–7. <https://doi.org/10.1007/BF02913365>.
- [66] Tateyama Y, Ohno T. Atomic-scale effects of hydrogen in iron toward hydrogen embrittlement: ab-initio study. *ISIJ Int*

- 2003;43:573–8. <https://doi.org/10.2355/isijinternational.43.573>.
- [67] Fukai Y. The metal-hydrogen system. <https://doi.org/10.1007/3-540-28883-X>; 2005.
- [68] Oriani RA. Hydrogen embrittlement of steels. *Annu Rev Mater Sci* 1978;8:327–57. <https://doi.org/10.1016/B978-044452787-5.00200-6>.
- [69] Krom AHM, Bakker A, Koers RWJ. Modelling hydrogen-induced cracking in steel using a coupled diffusion stress finite element analysis. *Int J Pres Ves Pip* 1997;72:139–47. [https://doi.org/10.1016/S0308-0161\(97\)00019-7](https://doi.org/10.1016/S0308-0161(97)00019-7).
- [70] Zhou L, Zhou Y. Determination of compressibility factor and fugacity coefficient of hydrogen in studies of adsorptive storage. *Int J Hydrogen Energy* 2001;26:597–601. [https://doi.org/10.1016/S0360-3199\(00\)00123-3](https://doi.org/10.1016/S0360-3199(00)00123-3).
- [71] Tkacz M, Litwiniuk A. Useful equations of state of hydrogen and deuterium. *J Alloys Compd* 2002;330–332:89–92. [https://doi.org/10.1016/S0925-8388\(01\)01488-8](https://doi.org/10.1016/S0925-8388(01)01488-8).
- [72] Hemmes H, Driessen A, Griessen R. Thermodynamic properties of hydrogen at pressures up to 1 Mbar and temperatures between 100 and 1000K. *J Phys C Solid State Phys* 1986;19:3571–85. <https://doi.org/10.1088/0022-3719/19/19/013>.
- [73] Michels A, De Graaff W, Wassenaar T, Levelt JMH, Louwse P. Compressibility isotherms of hydrogen and deuterium at temperatures between -175 °C and +150 °C (at densities up to 960 Amagat). *Physica* 1959;25:25–42.
- [74] Drexler A, Bergmann C, Manke G, Kokotin V, Mraczek K, Leitner S, Pohl M, Ecker W. Local hydrogen accumulation after cold forming and heat treatment in punched advanced high strength steel sheets. *J Alloys Compd* 2021;856:158226. <https://doi.org/10.1016/j.jallcom.2020.158226>.
- [75] Krom AHM, Bakker A. Hydrogen trapping models in steel. *Metall Mater Trans B* 2000;31:1475–82. <https://doi.org/10.1007/s11663-000-0032-0>.
- [76] Brunbauer S, Winter G, Antretter T, Staron P, Ecker W. Residual stress and microstructure evolution in steel tubes for different cooling conditions – simulation and verification. *Mater Sci Eng* 2019;747:73–9. <https://doi.org/10.1016/j.msea.2019.01.037>.